NANO LETTERS

Letter

pubs.acs.org/NanoLett

Transitions from Near-Surface to Interior Redox upon Lithiation in Conversion Electrode Materials

Kai He,[†] Huolin L. Xin,[†] Kejie Zhao,[‡] Xiqian Yu,[§] Dennis Nordlund,[∥] Tsu-Chien Weng,[∥] Jing Li,[†,⊥] Yi Jiang,[#] Christopher A. Cadigan,[▽] Ryan M. Richards,[▽] Marca M. Doeff,[○] Xiao-Qing Yang,[§] Eric A. Stach,[†] Ju Li,*[,‡] Feng Lin,*[,▽,○] and Dong Su*[,†,⊥]

[†]Center for Functional Nanomaterials, Brookhaven National Laboratory, Upton, New York 11973, United States

[‡]Department of Nuclear Science and Engineering and Department of Materials Science and Engineering, Massachusetts Institute of Technology, Cambridge, Massachusetts 02139, United States

[§]Chemistry Department, Brookhaven National Laboratory, Upton, New York 11973, United States

[∥]Stanford Synchrotron Radiation Lightsource, SLAC National Accelerator Laboratory, Menlo Park, California 94025, United States

[⊥]Department of Materials Science and Engineering, Stony Brook University, Stony Brook, New York 11794, United States

[#]Department of Physics, Cornell University, Ithaca, New York 14853, United States

[▽]Department of Chemistry and Geochemistry, Materials Science Program, Colorado School of Mines, Golden, Colorado 80401, United States

[○]Environmental Energy Technologies Division, Lawrence Berkeley National Laboratory, Berkeley, California 94720, United States

Supporting Information

ABSTRACT: Nanoparticle electrodes in lithium-ion batteries have both near-surface and interior contributions to their redox capacity, each with distinct rate capabilities. Using combined electron microscopy, synchrotron X-ray methods and ab initio calculations, we have investigated the lithiation pathways that occur in NiO electrodes. We find that the near-surface electroactive ($Ni^{2+} \rightarrow Ni^{0}$) sites saturated very quickly, and then encounter unexpected difficulty in propagating the phase transition into the electrode (referred to as a "shrinking-core" mode). However, the interior capacity for $Ni^{2+} \rightarrow Ni^{0}$ can be accessed efficiently following the nucleation of lithiation "fingers" that propagate into the sample bulk, but only after a certain incubation time. Our microstructural observations of the transition from a slow shrinking-core mode to a faster lithiation finger mode corroborate with synchrotron characterization of large-format batteries and can be rationalized by stress effects on transport at high-rate discharge. The finite incubation time of the lithiation fingers sets the intrinsic limitation for the rate capability (and thus the power) of NiO for electrochemical energy storage devices. The present work unravels the link between the nanoscale reaction pathways and the C-rate-dependent capacity loss and provides guidance for the further design of battery materials that favors high C-rate charging.

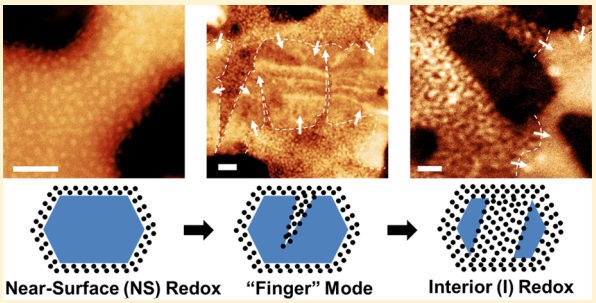

KEYWORDS: *Lithium ion battery, nickel oxide, conversion reaction, in situ TEM, incubation, rate capability*

Lithium-ion batteries and supercapacitors both rely on electrochemical redox processes, although different mechanisms determine their relative energy and power densities.[1−5] For nanostructured electrodes of lithium-ion batteries, the capacity contains contributions from redox reactions that occur in both the interior (I) and near-surface (NS) regions.[6−9] It is believed that the interior redox reactions contribute more to the overall battery capacity, but these take a longer time to be activated. In contrast, redox reactions in the near-surface reaction may exhibit a supercapacitor-like behavior (i.e., a high power density) because of the short transport paths for ions and electrons.[7−9] Thus, an understanding of the kinetics of the transition from NS-redox to I-redox is critical to determining the rate capability of a lithium ion battery. Even though the rate capability and reaction kinetics can be improved by modifications to the material structure (such as surface coating and functionalization) and by architecture engineering,[10−21] it is still not clear how the redox front propagates into the interior, especially at high discharge rates.

In this work, we have integrated complementary atomic resolution transmission electron microscopy (TEM) imaging, electron and X-ray spectroscopies, and electrochemistry measurements to study the kinetics of the lithiation of NiO

Received: December 29, 2014
Revised: January 15, 2015
Published: January 29, 2015

DOI: 10.1021/nl5049884
Nano Lett. 2015, 15, 1437−1444

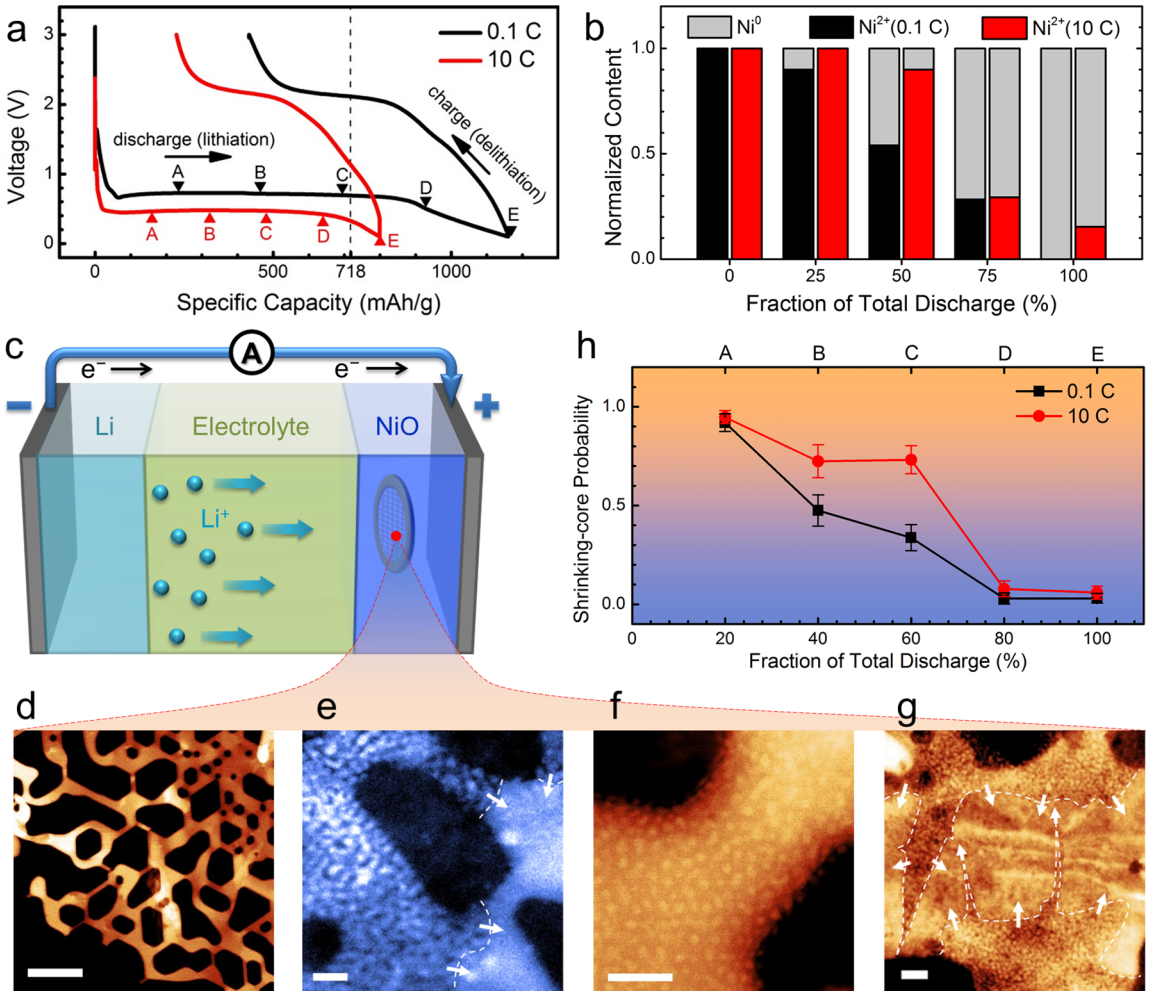

Figure 1. Electrochemical and structural change after lithiation of NiO nanosheets. (a) Charge−discharge curves at rates of 0.1C and 10C. Dashed line indicates the theoretical capacity of 718 mAh/g. (b) Relative content of Ni^{2+} and Ni^0 at different discharge fractions as measured by synchrotron Ni K-edge XAS (original spectra shown in Supporting Information Figure 2). (c) Schematic illustration of an ex situ battery cell with a TEM grid submerged in the active NiO electrode. ADF-STEM images of (d) a pristine NiO nanosheet, (e) an area that has almost been fully lithiated via the bulk mode (Mode B), (f) an area that has been partially lithiated only on surface via the shrinking-core mode (Mode S), and (g) an area that has been partially lithiated via the finger mode (Mode F). Dashed lines and arrows indicate reaction fronts and propagation directions. (h) Probability of surface mode as a function of discharge fraction via 0.1C and 10C discharges. The data points are acquired at the corresponding states labeled A−E in (a). Scale bars, 100 (d), 10 (e,f), and 20 nm (g).

nanosheet electrodes. After visualizing the heterogeneous redox reaction modes at the near-surface and interior regions, we found that the transition from NS-redox to I-redox reaction is exceptionally slow when it occurs through the classic "shrinking-core" mode.[22] Instead, most of the interior $Ni^{2+} \rightarrow Ni^0$ sites are mined only after high-aspect-ratio "reaction fingers" are nucleated. These subsequently penetrate deeply into the nanoparticle interior and then thicken so as to spread the transition through the bulk of the material. There is an "incubation" time, which averages to about 100 s from in situ TEM observations, before the redox reaction can penetrate into the interior. The reaction time scale and patterns we discovered from in situ TEM correlate with the ultimate rate performance of large-format batteries and are further supported by ex situ TEM and X-ray spectroscopies. We believe such heterogeneous transition mechanisms from NS-redox to I-redox may be generic and transferrable to a large class of conversion nanoelectrode materials.

Our experiments were performed using three setups: (I) 2032-type coin cells (Figure 1a,b) using liquid electrolyte, (II) TEM "grid-in-a-coin-cell" using liquid electrolyte for easy post-mortem TEM characterization of large-format batteries (Figure 1c−g), and (III) in situ lithiation (Figure 2, 3) using Li_2O solid electrolyte. Setups I, II, and III all use the same NiO nanosheets with holes and faceted surfaces[23,24] as positive electrodes, and Li metal as negative electrodes. For battery performance, the initial formatting cycle is crucial, as the structures inherited from the first cycle may dramatically influence subsequent cycles for conversion electrodes.[25] Therefore, the first cycle, specifically the first lithiation process, as shown in reaction eq 1[26,27] and confirmed by in situ diffraction (Supporting Information Figure S1 and Movie 4), is the focus of the present paper.

$$NiO + 2Li^+ + 2e^-(U) \rightarrow Ni + Li_2O \quad (1)$$

For setup I, the voltage-total capacity curves are shown in Figure 1a for high (~10C) and low (~0.1C) charging rate, respectively. The nominal first-cycle discharge (lithiation) capacities obtained at 10C (800 mAh/g) and 0.1C (1160 mAh/g) are both larger than the theoretical specific capacity

DOI: 10.1021/nl5049884
Nano Lett. 2015, 15, 1437−1444

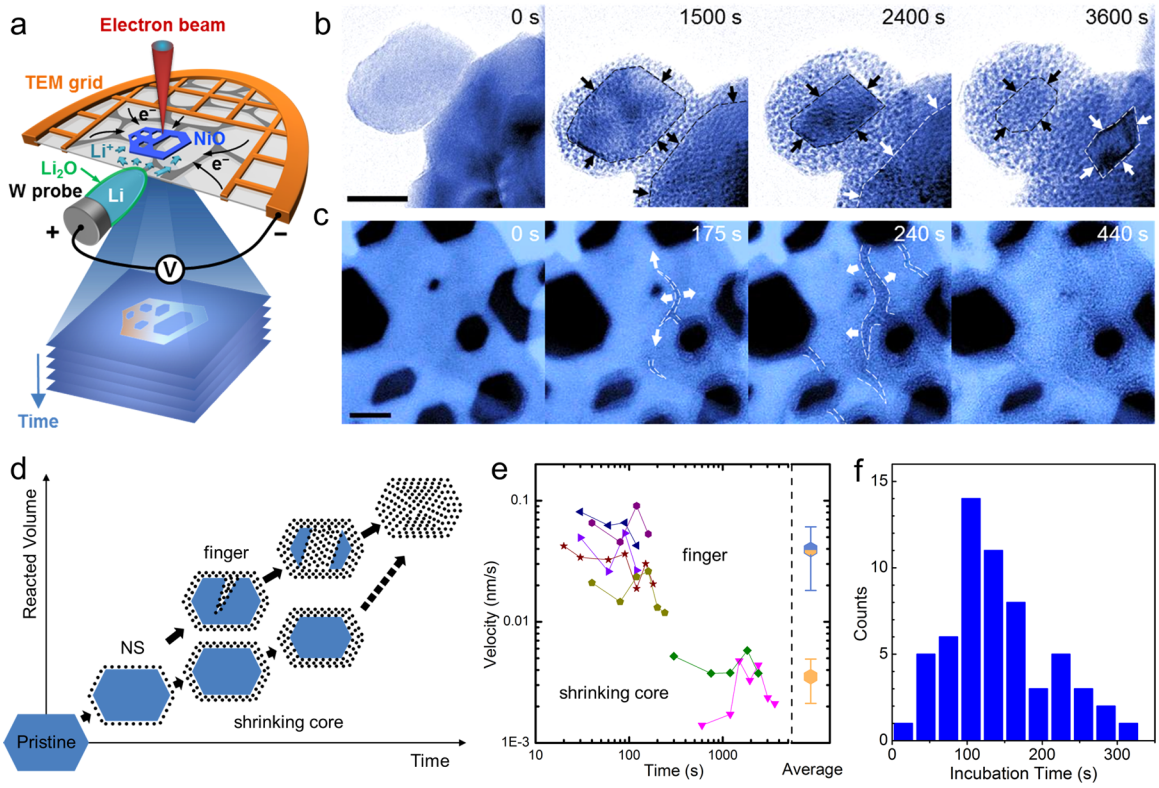

Figure 2. Structural evolution during in situ lithiation of NiO nanosheets. (a) Schematic illustration of in situ electrochemical cell setup. Time-sequenced S/TEM snapshots during in situ lithiation indicate (b) shrinking-core mode, and (c) finger mode. Dashed lines and arrows indicate reaction fronts and propagation directions. (d) Schematic cartoon showing heterogeneous pathways of N → I transitions. (e) The velocity of reaction front propagation in different pathways deduced from numerous time-dependent position measurements (see Supporting Information Figure 6). The modality-correlated velocities exhibit in two groups and their average values are shown in the right panel. (f) Histogram showing statistics of incubation time from numerous finger-mode events. Scale bars, 20 nm.

(718 mAh/g) of NiO. This does not mean full conversion of $Ni^{2+} \rightarrow Ni^0$ centers,[28] however, due to electrolyte decomposition and SEI formation that consume injected electrons: these side reactions become possible for ethylene carbonate/diethyl carbonate liquid electrolyte whenever the voltage U drops below ~1.3 V against Li^+/Li (ref 3). To reveal the actual degree of $Ni^{2+} \rightarrow Ni^0$ conversion in the first discharge, we performed synchrotron hard X-ray absorption spectroscopy[29,30] (XAS, Supporting Information Figure S2) that characterizes the valence state of all Ni atoms contained in a 2032 coin cell. The XAS spectra were fit to a linear combination of Ni^{2+} and Ni^0 spectroscopic components, and the degree of $Ni^{2+} \rightarrow Ni^0$ conversion is indicated in Figure 1b against the fraction of total discharge (FoTD). (Please note that FoTD includes side reactions.) It is interesting to note that at FoTD = 100% all the Ni^{2+} were reduced to Ni^0 in the 0.1C coin cell but in the 10C coin cell ~15% of the Ni^{2+} still remained unreduced. This means that at 10C not all the electroactive sites in NiO nanosheets can be reduced even as the voltage dropped to near zero against Li^+/Li (the equilibrium voltage of eq 1 is 0.6 V against Li^+/Li).[25] This measures the true rate-dependent electrodic capacity of NiO.

It is also interesting to note that very little Ni^{2+} was reduced up to FoTD = 25%, and 0.1C and 10C samples do not differ much in this regard (Figure 1b). This means electrolyte decomposition and SEI formation consume most of electrons injected up to the first quarter of discharge, which is reasonable since SEI formation happens below U = 1.3 V[3], earlier than U_0 = 0.6 V[25] for reaction 1. For 10C sample, even rather limited amount of Ni^{2+}/Ni^0 redox happened at the NS region (as observed by TEM), which is difficult to detect due to the low (surface) sensitivity of hard X-ray and the quantification technique using spectral linear combination. But SEI formation kinetics is self-slowing after the SEI thickness has grown. Generally speaking, SEI formation dominates the early part of the first discharge, and 0.1C sample forms more SEI than the 10C sample (1160−718=442 mAh/g vs 800−718 × 0.85=190 mAh/g, so almost double by the end of the discharge) overall due to the longer reaction time. For the later part of the first discharge, $Ni^{2+} \rightarrow Ni^0$ conversion dominates the total reaction. The difference between 0.1C and 10C samples in this regard is that while the degree of $Ni^{2+} \rightarrow Ni^0$ is almost linear between FoTD = 25−100% at 0.1C, for the 10C sample the $Ni^{2+} \rightarrow Ni^0$ reduction kinetics seems to have a nonlinear behavior. In the 10C sample, there is a small amount of conversion from FoTD = 25−50%, followed by very rapid conversion between FoTD = 50−75% ("inflection"). As 10C means 6 min at full discharge, this inflection stage is quite remarkable in the sense that more than 50% of all the Ni^{2+} in the coin cell is reduced in a time duration $\tau_{inflection}$ ~1.5 min. This indicates that certain intrinsic kinetics in NiO nanosheets[23,24] must be quite fast to be able to accomplish this at nearly a constant voltage ~0.4 V (this driving voltage U barely changed between FoTD = 0−75%). Thus, the "intrinsic" rate capability of NiO nanosheets[23,24] can be quite good.[6] But for the FoTD = 75−100%, for various reasons (e.g., electrolyte decomposition, long-range Li^+/electron transport disruptions, or another possible reason to be suggested later) the previously rapid "inflection" slowed down, even though the

DOI: 10.1021/nl5049884
Nano Lett. 2015, 15, 1437−1444

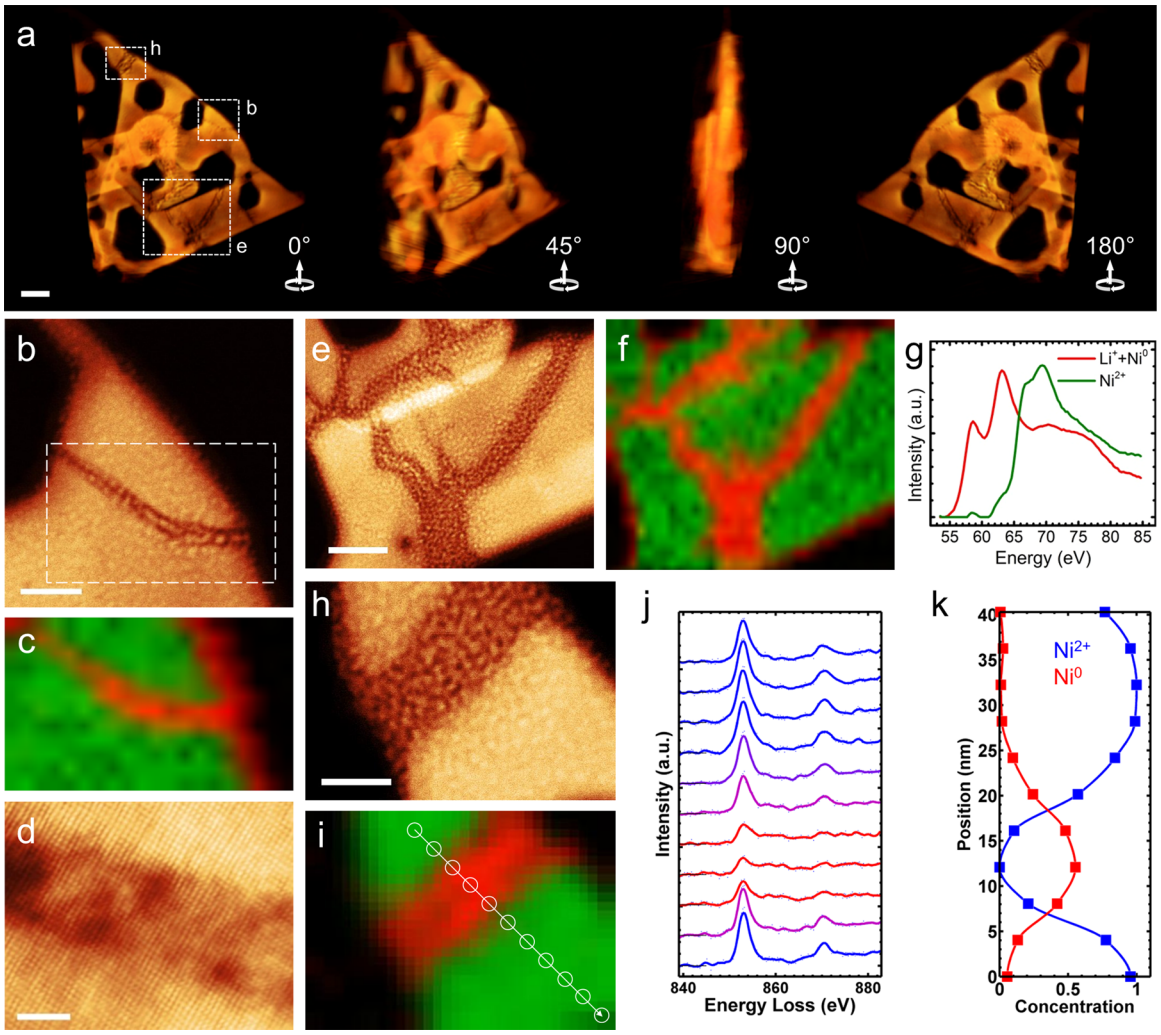

Figure 3. Tomography and EELS mapping of lithiated NiO fingers. (a) A series of reconstructed 3D tomograms from an in situ lithiated NiO nanosheet at viewing angles of 0°, 45°, 90°, and 180°, (also see Supporting Information Movie 5). (b,e,h) Zoom-in ADF-STEM images corresponding to the labeled regions in (a). (c,f) EELS mapping of Ni^{2+} (green) and Li^{+}+Ni^{0} (red) for areas in (b,e) using the low-loss spectra components shown in (g). (d) Atomically resolved STEM image showing a crack region coherently bounded with unlithiated NiO in (b). (i) EELS charge mapping of Ni^{2+} (green) and Ni^{0} (red) for the area in (h), a series of EELS spectra and $Ni^{2+/0}$ concentration profiles along the arrow are shown in (j,k), respectively. Scale bars, 20 (a), 10 (b), 2 (d), 20 (e), and 10 nm (h).

driving voltage U drops more rapidly in the last quarter of discharge and thus increases the reductive driving force. The $Ni^{2+} \rightarrow Ni^{0}$ conversion ended up unfinished, leaving behind 15% unreduced Ni^{2+}. Such nonlinear "incubation−inflection−saturation" coin-cell behavior at time scale of minutes may thus be attributed to an intrinsic NiO electrodic time scale, as opposed to the 0.1C case where the electron supply is throttled externally to be much slower than $\tau_{inflection}$.

We note that a redox time scale of minutes at 10C is on the borderline between what is nominally considered supercapacitor-like behavior and battery behavior ($\tau_{inflection}$ ~1.5 min would be considered fast in the battery context, but slow in the redox supercapacitor context). Conventional understanding of the operation of lithium ion batteries involves consideration of both near-surface electroactive sites and interior electroactive sites. However, there are few direct characterizations of either the NS or I behaviors and observations of the NS → I transition are few. In order to understand how discharge rate actually drives changes in the material's microstructure, we have utilized the TEM "grid-in-a-coin cell" method[23] as illustrated in Figure 1c (setup II). This approach allows us to subject NiO to states of charge that mimic the situation in a fully operational battery, yet are directly amenable to TEM imaging. The pristine NiO materials are ~20 nm thick sheets with closely packed {111} basal planes forming the largest free surfaces, and they are initially perforated with hexagonal holes that are bounded by {112} facets enabling short diffusion paths from NS to I redox sites (Figure 1d and Supporting Information Figure S3).[23,24] The uniform and thin thickness is natively electron-transparent and thus suitable for in situ TEM observations, particularly for large-scale in-plane lithiation propagation. The discharged samples usually contained a significant fraction of unreacted NiO (unreduced Ni^{2+}), with the reacted regions consisting of fine metallic Ni nanoparticles (Supporting Information Figure S4) embedded in a Li_2O matrix or covering the NiO surface (Figure 1e−g). Critically, for both C-rates we found three distinct, heterogeneous morphologies that differed in their relative amounts. The three lithiation modes are called Modes bulk (B), shrinking-core (S), and finger-like (F) and their appearance is described in detail below.

DOI: 10.1021/nl5049884
Nano Lett. 2015, 15, 1437−1444

In Mode B (bulk mode), the reaction front has advanced deeply inside the NiO interior (Figure 1e) with the reaction front normal $\mathbf{n} \perp [111]$. The reaction front is relatively flat, exhibits no strong crystallographic preference in its propagation direction (except for $\perp [111]$), and is sharply bounded by unreacted NiO. In Mode S (shrinking-core mode), the reaction appears to have first proceeded very rapidly along all surfaces by surface diffusion (later verified by in situ observations) and then thickens further uniformly perpendicular to all surfaces, including the (111) surfaces[22] (Figure 1f). Mode F (finger mode) exhibits a strikingly different morphology: a high-aspect-ratio lithiation finger $\perp [111]$ penetrates deep inside the unreacted material. Mode F has an overall appearance similar to that of a crack or wedge, although its microscopic manifestation is the reaction of NiO to Ni + Li_2O and not the cleavage of a material as would be observed in a crack (Figure 1g). In order to understand the correlation between the reaction morphology and the discharge rates, we imaged a large number of nanosheets reacted ex situ to a specified FoTD (20, 40, 60, 80, and 100%, corresponding to the points labeled A, B, C, D, and E in Figure 1a, respectively) at both 10C and 0.1C. Figure 1h summarizes the statistics obtained from the TEM images, which were collected in an unbiased manner (see an example in Supporting Information Figure S5). We see a distinct difference in the prevalence of different reaction morphologies as a function of the discharge rate: the high C-rate samples show a higher prevalence of Mode S (shrinking-core mode), while the low C-rate favors Mode B (bulk mode). Moreover, as the particle-ensemble FoTD advances, the 10C reaction morphology switched from being primarily Mode S to Mode B.

While a rigorous statistical link is established between the rate and the reaction modes at particles-ensemble level in Setup II, ex post facto imaging of this type cannot provide time-dependent trajectory of the NS → I reaction transition. In order to investigate this phenomenon further, we have utilized a real-time electron microscopy approach (Setup III) to investigate the reaction kinetics for the different modes. The in situ experiments utilized a dry electrochemical cell with no side reaction of organic electrolyte decomposition.[31−33] As illustrated in Figure 2a, Li ions are transferred toward the NiO electrode under a positive bias in a potentiostatic mode. In the in situ discharging experiments (Supporting Information Movies 1−2), even though there is no deliberate control of the discharge rates, we repeatedly and reproducibly observed the same reaction modes as in the ex situ cells (Figure 2b,c); this indicates that this in situ method is able to provide valid information that can be correlated with the ex post facto observations. In Figure 2b as well as Supporting Information Movie 1, we observed that the surface wetting is very fast by surface diffusion and the redox front propagates from the outer surface (after NS sites have been saturated). Such further propagation (via the shrinking core mode) encounters unexpected difficulty when trying to access the interior and proceeds rather slowly perpendicular to all surfaces of the nanosheet, including (111) surfaces.

However, we also found other pathways for the NS → I transition through the nucleation and subsequent growth of lithiation fingers, which occurred heterogeneously throughout the sheet (Figure 2c). The fingers initially nucleate on ⟨112⟩ facets randomly, a while after the near-surface sites saturate, then elongate $\perp [111]$ until the exits on the opposite surface of the NiO nanosheet. After penetrating all the way through, they then thicken into the nanosheet bulk. At the fully discharged state, the fingers have thickened enough to completely merge and therefore few identifiable fingers can be seen at FoTD = 100%. From the in situ observations, we found that Mode B occurred after the fingers in Mode F have thickened significantly and/or merged. We thus propose that Mode B occurs after the fingers have formed and thus facilitated Li^+/e^- supply through the interior. After the formation of fingers, the long-range transport capability through interior of the NiO nanosheets is improved and thus promotes the transition to Mode B. At no time were the nanosheets broken. This is in contrast to observations of true material fracture observed in Si nanoparticle[34,35] and ZnO nanowire[36] anode materials.

The complete picture of the reaction pathways for NiO nanosheets is depicted in Figure 2d, where two types of transitions from NS → I are observed: the shrinking-core mode and the finger mode, whereas the I → I transition is proceeded through bulk mode (Mode B, Supporting Information Movie 3). The fact that more Mode B events are observed in low-rate discharged sample implies that after more finger penetrations have been established the lithiation process is promoted. Using Supporting Information Movies 1 and 2, a quantitative analysis of the front propagation speed reveals a large difference between the shrinking-core and the finger modes, as shown in Figure 2e and Supporting Information Figure S6. After the finger has nucleated, the finger mode propagates at average speed of 0.045 nm/s, which is an order of magnitude faster than the shrinking-core mode. Therefore, we can deduce that the NS → I transition is more likely to happen via the finger mode than the shrinking-core mode, after the surfaces have reached a point where the near-surface sites are fully saturated. There appears to be an energy barrier against NS → I transition, which is lower for the more heterogeneous finger mode than for the shrinking-core mode. Before the finger nucleates, there appears to be an incubation time; we saw that the fingers generally do not form immediately after saturation of the near surface sites. We have collected the statistics of finger nucleation, shown in Figure 2f, and found that the characteristic incubation time $\tau_{incubation}$, defined as the average time lapse for the first finger to appear after near-surface site saturation in an area containing 1 hole on average (taken to be the characteristic in-plane length scale of the NiO nanosheet, around 30 nm), is ∼100 s. During the incubation, Li ions were transported to an interior redox site at near-surface and accumulated until nucleating a lithiation finger. This single-particle time scale matches reasonably well with the aforementioned coin-cell intrinsic time scale $\tau_{incubation}$ ∼ 1.5 min (FoTD = 0−25%) for Setup I. Therefore, a possible interpretation of the XAS results in Figure1b is that in our coin-cell particle ensemble, after the surface/interfacial transport channels are activated and saturated, it takes time for the fingers to nucleate, elongate, and thicken to access the interior capacity. At 0.1C (36 000 s for a full discharge), there is plenty of time for fingers to nucleate, so the microstructural evolution is throttled externally by electron supply. But at 10C (360 s discharge) a significant fraction of the characteristic in-plane areas will not be able to incubate even one finger due to the intrinsic time scale limitation of $\tau_{incubation}$, and therefore some Ni^{2+} can remain unreduced at FoTD = 100% even as the voltage is drastically lowered. With this assumption, the natural demarcation on the time axis to separate supercapacitor-like behavior from battery-like behavior would be $\tau_{discharge}$ ∼ 100 s, or around 30C. This means that the interior capacity can only be substantially utilized for galvanostatic rates slower than 30C; otherwise only the near-surface capacity can be utilized. A

DOI: 10.1021/nl5049884
Nano Lett. 2015, 15, 1437−1444

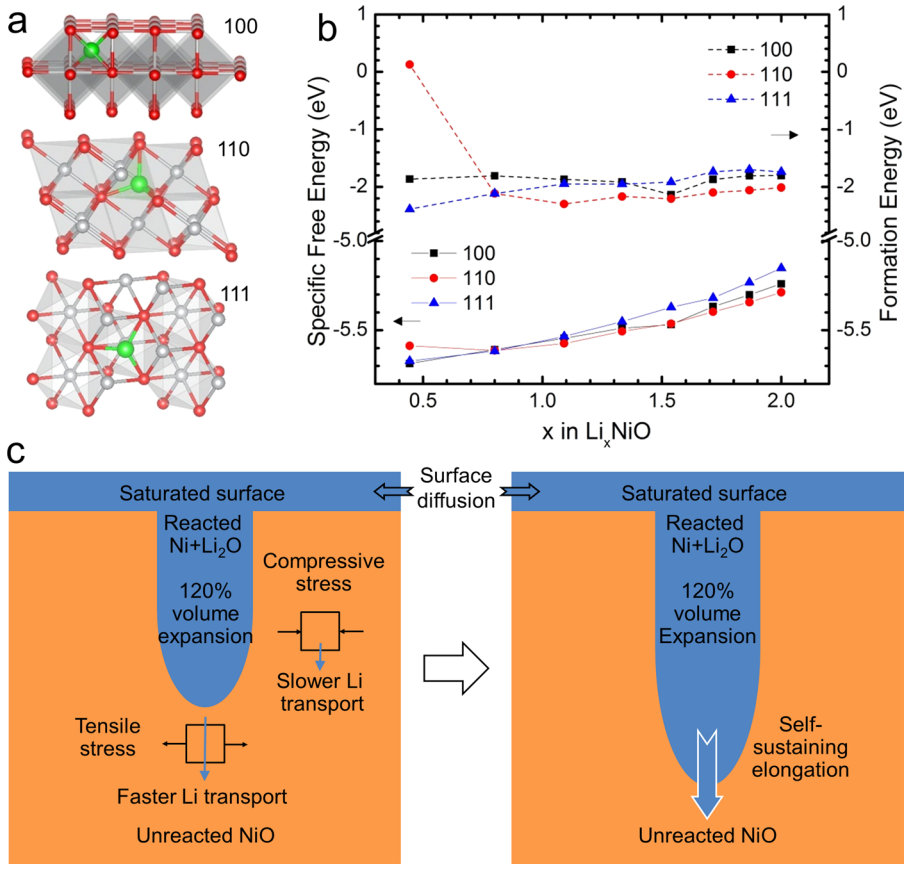

Figure 4. First-principles calculations and stress-induced growth. (a) The geometric feature of crystalline NiO for a lithium atom transport along the ⟨100⟩, ⟨110⟩, and ⟨111⟩ directions (Ni-gray, O-red, Li-green). (b) Formation energy and specific free energy as a function of lithium content when NiO is lithiated along the ⟨100⟩, ⟨110⟩, and ⟨111⟩ orientations. (c) Illustration of stress-induced self-sustaining finger growth.

verifiable prediction from our theory is therefore that if the galvanostatic rate is higher than 30C, our NiO nanosheets can only be used in the "supercapacitor" fashion, meaning that they exhibit a much reduced capacity (viewed in the battery context), even if the long-range transport limitation associated with Li ion in organic electrolyte were to be removed.[37] The intrinsic kinetic time scale extracted from our in situ TEM, $\tau_{incubation}$, does seem to match both our own coin-cell data as well as the general understanding of how NiO should perform at high rates.[37]

In order to understand the finger nucleation and propagation processes in more detail, we utilized analytical scanning transmission electron microscopy (STEM) to study the Mode F regions immediately following their formation. Reconstructed three-dimensional (3D) STEM electron tomograms clearly show that the Mode F reaction fronts form deep 3D penetrations into the NiO slab (Figure 3a and Supporting Information Movie 5). High-magnification STEM images (Figure 3b,e,h) indicate that fingers nucleate and grow into the sample bulk only after the local surfaces have fully saturated. We further explored the reaction chemistry at the nanoscale through electron energy-loss spectroscopic (EELS) mapping (Figure 3c,f,i). These maps indicate that both metallic Ni^0 and Li^+ are present at the sample surface and within the penetration grooves (finger regions). In addition, we have captured an early phase finger groove at atomic resolution as shown in Figure 3d.

From both ex situ and in situ TEM experiments, we observed that the lithiation of NiO disfavors propagation along ⟨111⟩. To interpret this, using ab initio calculations based on density functional theory, we calculated the formation energies and the migration energies along the ⟨100⟩, ⟨110⟩, and ⟨111⟩ directions at various Li concentrations (Figure 4a,b). We found that Li^+ transport along ⟨100⟩ and ⟨110⟩ directions is preferred. From the structural view shown in Figure 4a, it is thus plausible that Li ions transport more readily along in-plane orientations (⟨100⟩ and ⟨110⟩) where open channels are available for Li-ion insertion, whereas the diffusion pathway along the ⟨111⟩ orientation is blocked by front neighbor atoms.

Given that full lithiation can generate a volumetric strain up to 120% (Supporting Information Figure S7), the finger mode may be interpreted as a spontaneous symmetry-breaking instability (Figure 4c) in which the effect of self-stress on Li-ion diffusion plays a key role in perpetuating the long-aspect ratio growth, until the lithiation finger reaches the opposite surface, at which point it has to thicken. In contrast, the slow kinetics of the shrinking-core mode can be understood from a finite deformation model (Supporting Information Figure S8 and S9). In the circumferential (or core−shell) mode, the material is under three-dimensional constraints, which induces a triaxial stress field. This regulates the reaction in a more significant manner. This is consistent with recent studies that showed that a sufficiently large pressure at the interface of crystalline silicon could stop the lithiation reaction.[38] Stress, which is closely related to grain boundaries and other structural defects, may also affect short-range electron transfer[39] and phase boundary mobility,[40] and stress-relief induced contact network disruptions can alter the long-range transport routes of electrons and ions. Thus, the overall evolution can be quite

DOI: 10.1021/nl5049884
Nano Lett. 2015, 15, 1437−1444

complicated in an actual battery where conductive carbon black, binder, and the size and morphology of active material particles and the presence of the SEI all could play significant roles. Nonetheless, we believe the intrinsic electrodic time scale limitation measured by both our in situ, and post-mortem method, $\tau_{incubation}$ ~100 s and $\tau_{inflection}$ ~1.5 min, has an important bearing on both "high-rate" batteries as well as potentially on "low-rate" redox supercapacitors. We also identified that local stresses can be used to improve reaction kinetics, which can be leveraged as a new design rule for electrode materials engineering for high C-rate lithium ion battery systems. Our findings of surface-to-bulk phenomenon and rate-dependent lithiation mechanisms in NiO system could be generically applicable to conversion electrode materials, though optimization of morphologies, facets, and sizes may be further helpful to improve redox kinetics.

Methods. *Sample Preparation.* The active material (NiO nanosheets) was synthesized using a solvothermal method aided with an alcohol pseudosupercritical drying technique.[24] $Ni(NO_3)_2{\cdot}6H_2O$, urea, and benzyl alcohol were added into 50 mL of methanol with a molar ratio of 2:1:4. The solution was stirred for 1 h and transferred to an autoclave (Parr Reactor, model 4520). The reaction mixture was purged with Ar for 1 min and then Ar was filled with a pressure of 9 bar before initiating the heating process. The mixture was heated to 265 °C and maintained for 1.5 h. Finally, the vapor inside was vented (i.e., pseudosupercritical drying process). A green powder was collected and subsequently calcined at 500 °C for 6 h to yield NiO nanosheets.

Electrochemical Measurements. Composite electrodes were prepared with 80 wt % active material, 10 wt % polyvinylidene fluoride (PVDF), and 10 wt % acetylene carbon black in *N*-methyl-2-pyrrolidone (NMP) and cast onto copper current collectors. The 2032-type coin cells were assembled in an argon-filled glovebox using the composite electrode as the positive electrode and Li metal as the negative electrode. A Celgard separator 2400 and 1 M $LiPF_6$ electrolyte solution in 1:1 w/w ethylene carbonate/diethyl carbonate were used to fabricate coin cells. Battery testing was performed on a computer controlled VMP3 channels (BioLogic). 1C was defined as full discharging NiO in 1 h, which corresponds to a theoretical specific current density of 718 mA/g.

Synchrotron XAS. Ni K-edge XAS measurements were carried out at beamline X18A (NSLS, BNL) in transmission mode using a Si (111) double-crystal monochromator detuned to the 35% value of its original maximum intensity to eliminate the high order harmonics.[28] X-ray absorption near edge structure data was analyzed by ATHENA software package. The linear combination fitting by using the spectra of two end members (NiO and Ni) as the standards achieved the accurate Li stoichiometry in Li_xNiO_2 at each reaction stage, illustrated by Figure 1b.

TEM Characterization. The in situ TEM electrochemical cell was incorporated into a Nanofactory TEM-STM specimen holder (Figure 2a) in which NiO nanosheets dispersed onto a TEM half-grid with amorphous carbon support are analogous to the NiO-C composite electrode, Li metal is coated onto a piezo-driven W probe as the counter electrode with a thin layer of Li_2O formed on Li metal as the solid electrolyte. The Li and NiO were loaded onto the holder in an Ar-filled glovebox and then transferred to TEM column using a sealed Ar bag to avoid air exposure. During the in situ electrochemical tests, a constant negative dc potential was applied to NiO electrode against the Li source during the lithiation process, and the lithiation processes were captured by real-time imaging in either TEM or STEM mode. Electron tomography of the in situ lithiated sample was acquired in ADF-STEM mode with tilt series from −70° to 70° and 1° intervals. The ex situ samples after discharge in coin cells were examined at a large number of lithiated locations to reveal statistical probability of surface or bulk reaction modalities. The total area we checked for each sample was about a few hundreds of micrometers by a few hundreds of micrometers. The in situ measurements and tomography were performed on a JEOL 2100F TEM operated at 200 kV. The high-resolution imaging and analytical EELS were conducted on a Hitachi HD2700C STEM operated at 200 kV and equipped with a probe aberration corrector (spatial resolution <1 Å, energy resolution 0.35 eV). The 3D tomography was reconstructed using the e^-Tomo software suite written by Robert Hovden et al. (Cornell Muller group) and visualized by Avizo 6.3.

Theoretical Calculations. The first-principles calculations based on density functional theory were performed using Vienna ab initio simulation package (VASP). The projector-augmented wave pseudopotentials were employed and the general gradient approximation for the exchange-correlation functional was used. We construct the crystalline NiO models of [100]-[010]-[001] and [$\bar{1}$10]- [111]- [11$\bar{2}$] orientations, which contain 96 atoms with periodic boundary conditions. The atomic structures and system energy are calculated with an energy cutoff of 400 eV. In energy optimization calculations, the atomic coordinates, the supercell shape, and volume were relaxed. The energy optimization was considered complete when the magnitude of the force on each atom was smaller than 0.04 eV $Å^{-1}$.

Finite element analysis and simulations based on continuum theory of finite deformation were performed both analytically and numerically using COMSOL Multiphysics software suites; for details see Supporting Information.

■ ASSOCIATED CONTENT

Supporting Information

Additional details of S/TEM, XAS, DFT calculation, and in situ movies. This material is available free of charge via the Internet at http://pubs.acs.org.

■ AUTHOR INFORMATION

Corresponding Authors

*E-mail: (J.L.) liju@mit.edu.
*E-mail: (F.L.) flin@lbl.gov.
*E-mail: (D.S.) dsu@bnl.gov.

Author Contributions

K.H. and H.L.X. contributed equally to this project.

K.H., H.L.X., F.L., and D.S. conceived and designed the experiments. K.H. and D.S. performed the in situ and ex situ S/TEM experiments. H.L.X. performed electron tomography and EELS acquisition and analysis. F.L., X.Y., and X.-Q.Y. performed the electrochemical measurements. K.Z. and Ju L. performed the theoretical modeling. F.L., X.Y., X.-Q.Y., D.N., and T.-C.W. performed the synchrotron X-ray measurements. C.A.C., F.L., and R.M.R. synthesized the NiO samples. Jing L. participated in data analysis. Y.J. participated in tomography reconstruction. K.H., H.L.X., Ju L., F.L., and D.S. discussed the scope of the manuscript. K.H. prepared the figures. K.H., D.S., Ju L., H.L.X., F.L., and E.A.S. wrote the manuscript with help

DOI: 10.1021/nl5049884
Nano Lett. 2015, 15, 1437−1444

from M.M.D., K.H., and H.L.X. contributed equally to this project. D.S. supervised the project. All authors participated in discussion of the results.

Notes

The authors declare no competing financial interest.

■ ACKNOWLEDGMENTS

The electron microscopy work (S/TEM, EELS, and tomography) was carried out at the Center for Functional Nanomaterials, Brookhaven National Laboratory, which is supported by the U.S. Department of Energy (DOE), Office of Basic Energy Sciences, under Contract No. DE-AC02-98CH10886 and DE-SC-00112704. The authors acknowledge the technical support from Dr. Steven N. Ehrlich at Beamline X18A of National Synchrotron Light Source at Brookhaven National Laboratory, as well as the support from Beamline 9-BM-B at APS. X.Y. and X.-Q.Y. were supported by the U.S. DOE, the Assistant Secretary for Energy Efficiency and Renewable Energy, Office of Vehicle Technologies under Contract No. DE-AC02-98CH10886 and DE-SC-00112704. The synchrotron X-ray work was partially carried out at the Stanford Synchrotron Radiation Lightsource, SLAC National Accelerator Laboratory, supported by the U.S. DOE under Contract No. DE-AC02-76SF00515. Y.J. is supported by DOE Grant DE-FG02-11ER16210. Ju L. acknowledges support by NSF DMR-1240933 and DMR-1120901. Computational time on the Extreme Science and Engineering Discovery Environment (XSEDE) under Grant TG-DMR130038 is gratefully acknowledged.

■ REFERENCES

(1) Tarascon, J. M.; Armand, M. *Nature* **2001**, *414*, 359−367.
(2) Whittingham, M. S. *Chem. Rev.* **2004**, *104*, 4271−4301.
(3) Goodenough, J. B.; Kim, Y. *Chem. Mater.* **2010**, *22*, 587−603.
(4) Arico, A. S.; Bruce, P.; Scrosati, B.; Tarascon, J. M.; Van Schalkwijk, W. *Nat. Mater.* **2005**, *4*, 366−377.
(5) Simon, P.; Gogotsi, Y.; Dunn, B. *Science* **2014**, *343*, 1210−1211.
(6) Kang, B.; Ceder, G. *Nature* **2009**, *458*, 190−193.
(7) Conway, B. E. *J. Electrochem. Soc.* **1991**, *138*, 1539−1548.
(8) Simon, P.; Gogotsi, Y. *Nat. Mater.* **2008**, *7*, 845−854.
(9) Wang, G.; Zhang, L.; Zhang, J. *Chem. Soc. Rev.* **2012**, *41*, 797−828.
(10) Kang, K.; Meng, Y. S.; Breger, J.; Grey, C. P.; Ceder, G. *Science* **2006**, *311*, 977−980.
(11) Doeff, M. M.; Hu, Y.; McLarnon, F.; Kostecki, R. *Electrochem. Solid-State Lett.* **2003**, *6*, A207−A209.
(12) Liu, H.; Strobridge, F. C.; Borkiewicz, O. J.; Wiaderek, K. M.; Chapman, K. W.; Chupas, P. J.; Grey, C. P. *Science* **2014**, *344*, 1252817.
(13) Xu, B.; Fell, C. R.; Chi, M.; Meng, Y. S. *Energy Environ. Sci.* **2011**, *4*, 2223−2233.
(14) Fong, R.; von Sacken, U.; Dahn, J. R. *J. Electrochem. Soc.* **1990**, *137*, 2009−2013.
(15) Poizot, P.; Laruelle, S.; Grugeon, S.; Dupont, L.; Tarascon, J. M. *Nature* **2000**, *407*, 496−499.
(16) Hu, Y. S.; Guo, Y. G.; Sigle, W.; Hore, S.; Balaya, P.; Maier, J. *Nat. Mater.* **2006**, *5*, 713−717.
(17) Bruce, P. G.; Scrosati, B.; Tarascon, J. M. *Angew. Chem., Int. Ed.* **2008**, *47*, 2930−2946.
(18) Lee, K. T.; Cho, J. *Nano Today* **2011**, *6*, 28−41.
(19) Chan, C. K.; Peng, H.; Liu, G.; McIlwrath, K.; Zhang, X. F.; Huggins, R. A.; Cui, Y. *Nat. Nanotechnol.* **2008**, *3*, 31−35.
(20) Liu, N.; Lu, Z.; Zhao, J.; McDowell, M. T.; Lee, H. W.; Zhao, W.; Cui, Y. *Nat. Nanotechnol.* **2014**, *9*, 187−192.
(21) Zheng, G.; Lee, S. W.; Liang, Z.; Lee, H. W.; Yan, K.; Yao, H.; Wang, H.; Li, W.; Chu, S.; Cui, Y. *Nat. Nanotechnol.* **2014**, *9*, 618−623.
(22) Srinivasan, V.; Newman, J. *J. Electrochem. Soc.* **2004**, *151*, A1517−A1529.
(23) Lin, F.; Nordlund, D.; Weng, T. C.; Zhu, Y.; Ban, C.; Richards, R. M.; Xin, H. L. *Nat. Commun.* **2014**, *5*, 3358.
(24) Hu, J.; Zhu, K.; Chen, L.; Yang, H.; Li, Z.; Suchopar, A.; Richards, R. *Adv. Mater.* **2008**, *20*, 267−271.
(25) Cabana, J.; Monconduit, L.; Larcher, D.; Palacin, M. R. *Adv. Mater.* **2010**, *22*, E170−E192.
(26) Varghese, B.; Reddy, M. V.; Zhu, Y.; Lit, C. S.; Hoong, T. C.; Rao, G. V. S.; Chowdari, B. V. R.; Wee, A. Y. S.; Lim, C. T.; Sow, C. H. *Chem. Mater.* **2008**, *20*, 3360−3367.
(27) Zhou, G.; Wang, D. W.; Yin, L. C.; Li, N.; Li, F.; Cheng, H. M. *ACS Nano* **2012**, *6*, 3214−3223.
(28) Hu, Y. Y.; Liu, Z.; Nam, K. W.; Borkiewicz, O. J.; Cheng, J.; Hua, X.; Dunstan, M. T.; Yu, X.; Wiaderek, K. M.; Du, L. S.; Chapman, K. W.; Chupas, P. J.; Yang, X. Q.; Grey, C. P. *Nat. Mater.* **2013**, *12*, 1130−1136.
(29) Yu, X.; Lyu, Y.; Gu, L.; Wu, H.; Bak, S. M.; Zhou, Y.; Amine, K.; Ehrlich, S. N.; Li, H.; Nam, K. W.; Yang, X. Q. *Adv. Energy Mater.* **2014**, *4*, 1300950.
(30) Chueh, W. C.; Gabaly, F. E.; Sugar, J. D.; Bartelt, N. C.; McDaniel, A. H.; Fenton, K. R.; Zavadil, K. R.; Tyliszczak, T.; Lai, W.; McCarty, K. F. *Nano Lett.* **2013**, *13*, 866−872.
(31) He, K.; Zhou, Y.; Gao, P.; Wang, L.; Pereira, N.; Amatucci, G. G.; Nam, K. W.; Yang, X. Q.; Zhu, Y.; Wang, F.; Su, D. *ACS Nano* **2014**, *8*, 7251−7259.
(32) Liu, X. H.; Wang, J. W.; Huang, S.; Fan, F.; Huang, X.; Liu, Y.; Krylyuk, S.; Yoo, J.; Dayeh, S. A.; Davydov, A. V.; Mao, S. X.; Picraux, S. T.; Zhang, S.; Li, J.; Zhu, T.; Huang, J. Y. *Nat. Nanotechnol.* **2012**, *7*, 749−756.
(33) Gu, M.; Kushima, A.; Shao, Y.; Zhang, J. G.; Liu, J.; Browning, N. D.; Li, J.; Wang, C. *Nano Lett.* **2013**, *13*, 5203−5211.
(34) McDowell, M. T.; Ryu, I.; Lee, S. W.; Wang, C.; Nix, W. D.; Cui, Y. *Adv. Mater.* **2012**, *24*, 6034−6041.
(35) Liu, X. H.; Liu, Y.; Kushima, A.; Zhang, S.; Zhu, T.; Li, J.; Huang, J. Y. *Adv. Energy Mater.* **2012**, *2*, 722−741.
(36) Kushima, A.; Liu, X. H.; Zhu, G.; Wang, Z. L.; Huang, J. Y.; Li, J. *Nano Lett.* **2011**, *11*, 4535−4541.
(37) Feng, L.; Zhu, Y.; Ding, H.; Ni, C. *J. Power Sources* **2014**, *267*, 430−444.
(38) Zhao, K.; Pharr, M.; Wan, Q.; Wang, W. L.; Kaxiras, E.; Vlassak, J. J.; Suo, Z. *J. Electrochem. Soc.* **2012**, *159*, A238−A243.
(39) Bai, P.; Bazant, M. Z. *Nat. Commun.* **2014**, *5*, 3585.
(40) Yang, H.; Huang, S.; Huang, X.; Fan, F.; Liang, W.; Liu, X. H.; Chen, Q. L.; Huang, J. Y.; Li, J.; Zhu, T.; Zhang, S. *Nano Lett.* **2012**, *12*, 1953−1958.

DOI: 10.1021/nl5049884
Nano Lett. 2015, 15, 1437−1444

Supporting Information

Transitions from Near-Surface to Interior Redox upon Lithiation in Conversion Electrode Materials

Kai He[†,¶], Huolin L. Xin[†,¶], Kejie Zhao[‡], Xiqian Yu[§], Dennis Nordlund[‖], Tsu-Chien Weng[‖], Jing Li[†,⊥], Yi Jiang[#], Christopher A. Cadigan[▽], Ryan M. Richards[▽], Marca M. Doeff[○],Xiao-Qing Yang[§], Eric A. Stach[†], Ju Li[‡,*], Feng Lin[▽,○,*], and Dong Su[†,⊥,*]

[†]Center for Functional Nanomaterials, Brookhaven National Laboratory, Upton, New York 11973, USA.

[‡]Department of Materials Science and Engineering, Massachusetts Institute of Technology, Cambridge, Massachusetts 02139, USA.

[§]Chemistry Department, Brookhaven National Laboratory, Upton, New York 11973, USA.

[‖]Stanford Synchrotron Radiation Lightsource, SLAC National Accelerator Laboratory, Menlo Park, California 94025, USA.

[⊥]Department of Materials Science and Engineering, Stony Brook University, Stony Brook, New York 11794, USA.

[#]Department of Physics, Cornell University, Ithaca, New York 14853, USA.

[▽]Department of Chemistry and Geochemistry, Materials Science Program, Colorado School of Mines, Golden, Colorado 80401, USA.

[○]Environmental Energy Technologies Division, Lawrence Berkeley National Laboratory, Berkeley, California 94720, USA.

[¶]K.H. and H.L.X. contributed equally to this work.

*E-mails: liju@mit.edu; flin@lbl.gov; dsu@bnl.gov

Table of Contents

1. Supporting Figures S1-S6
2. Detailed discussion on the DFT calculation and finite element analysis (Figures S7-S9)
3. Description of Supporting Movies 1-5

1. Supporting Figures S1–S6

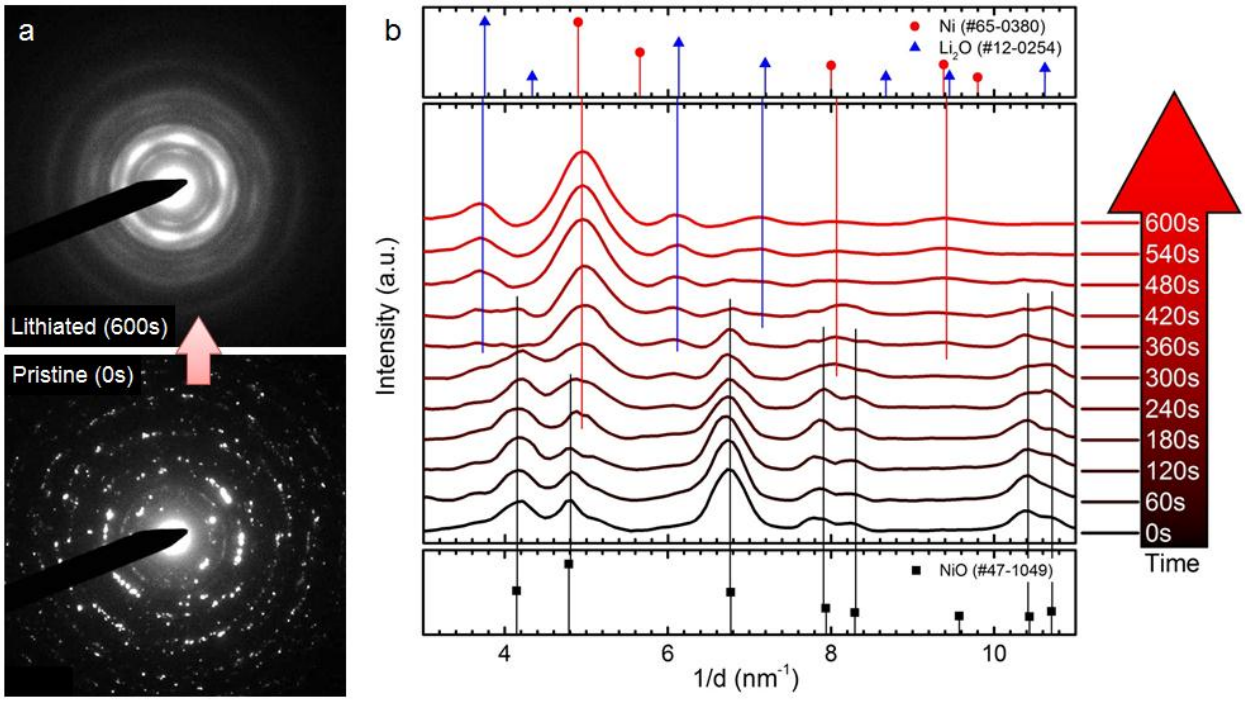

Figure S1. Phase evolution from *in situ* electron diffraction. A real-time video (Movie 4) was taken in the diffraction mode during an *in situ* lithiation process, and a series of frames (0 – 600 s, 60 s interval) were selected for phase identification. (a) Electron diffraction patterns of pristine (0 s) state and fully lithiated (600 s) states, showing a dramatic change from discrete sharp rings to continuous broad rings. (b) Intensity profiles (after background subtraction) of the rotationally averaged electron diffractions as a function of reaction time (0 to 600 s). The electron diffraction profiles are readily indexed to the standard NiO (#47-1049), Ni (#65-0380), and Li_2O (#12-0254) phases, which indicates the gradual phase transformation from the pristine NiO phase to Ni and Li_2O phases.

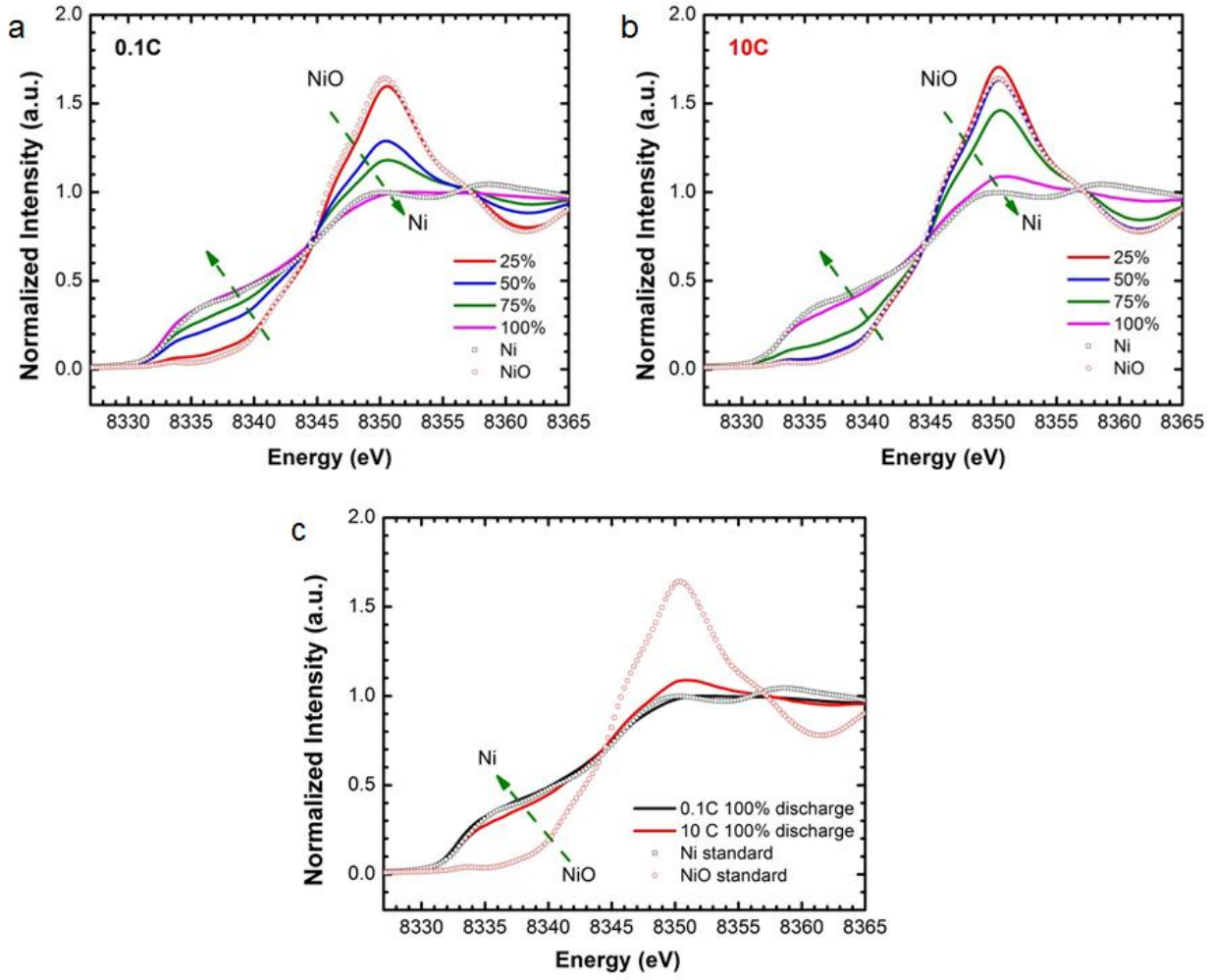

Figure S2. Synchrotron XAS at high and low charging rate. Hard X-ray absorption spectroscopy analysis for discharge rates of (a) 0.1 C and (b) 10 C, at different FoTD states (25%, 50%, 75%, and 100%). By fitting with a linear combination of standard Ni and NiO XAS profiles, the relative contents of Ni^0 and Ni^{2+} can be calculated, as plotted in Figure 1b. (c) Comparison of XAS profiles between 0.1 C and 10 C discharges at the final states. The 0.1 C discharge results in complete conversion to Ni, whereas the 10 C discharge shows that only 85% of NiO has been converted to Ni.

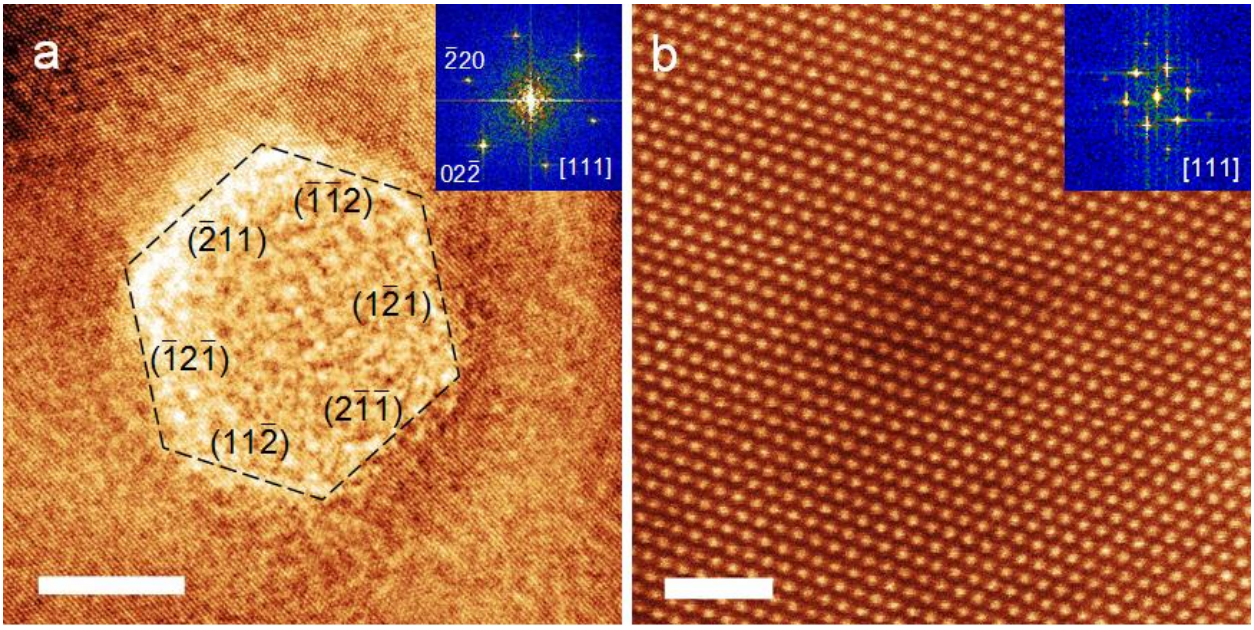

Figure S3. High-resolution imaging of pristine NiO. (a) High-resolution TEM image of the pristine NiO nanosheet with a hexagonal hole. The inset FFT shows the zone axis on the [111] direction. The inner edges of the hole are terminated at {112} planes. (b) High-resolution STEM image of the pristine NiO nanosheet. The inset FFT shows the zone axis on the [111] direction. Scale bars: (a) 5 nm, (b) 1 nm.

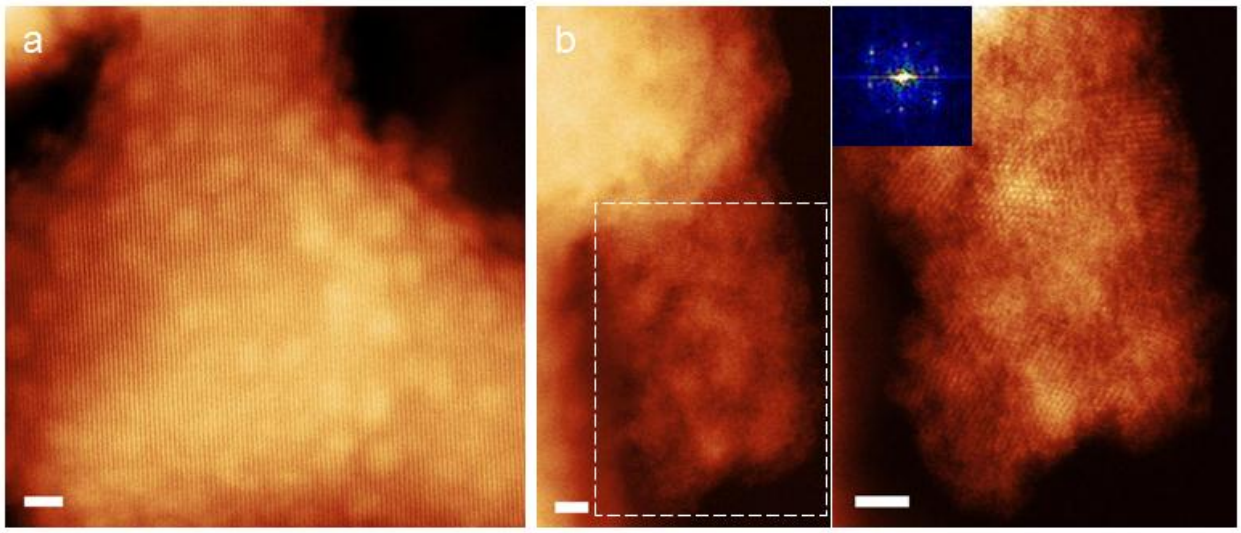

Figure S4. High-resolution STEM imaging after lithiation. (a) Morphology of Mode S (shrinking-core): separated Ni nanoparticles on the surface of NiO. (b) Morphology of Mode B (bulk): interconnected Ni nanoparticles fused into a cluster. The inset FFT indicates the [110] orientation of the Ni nanoparticles. Scale bars, 2 nm.

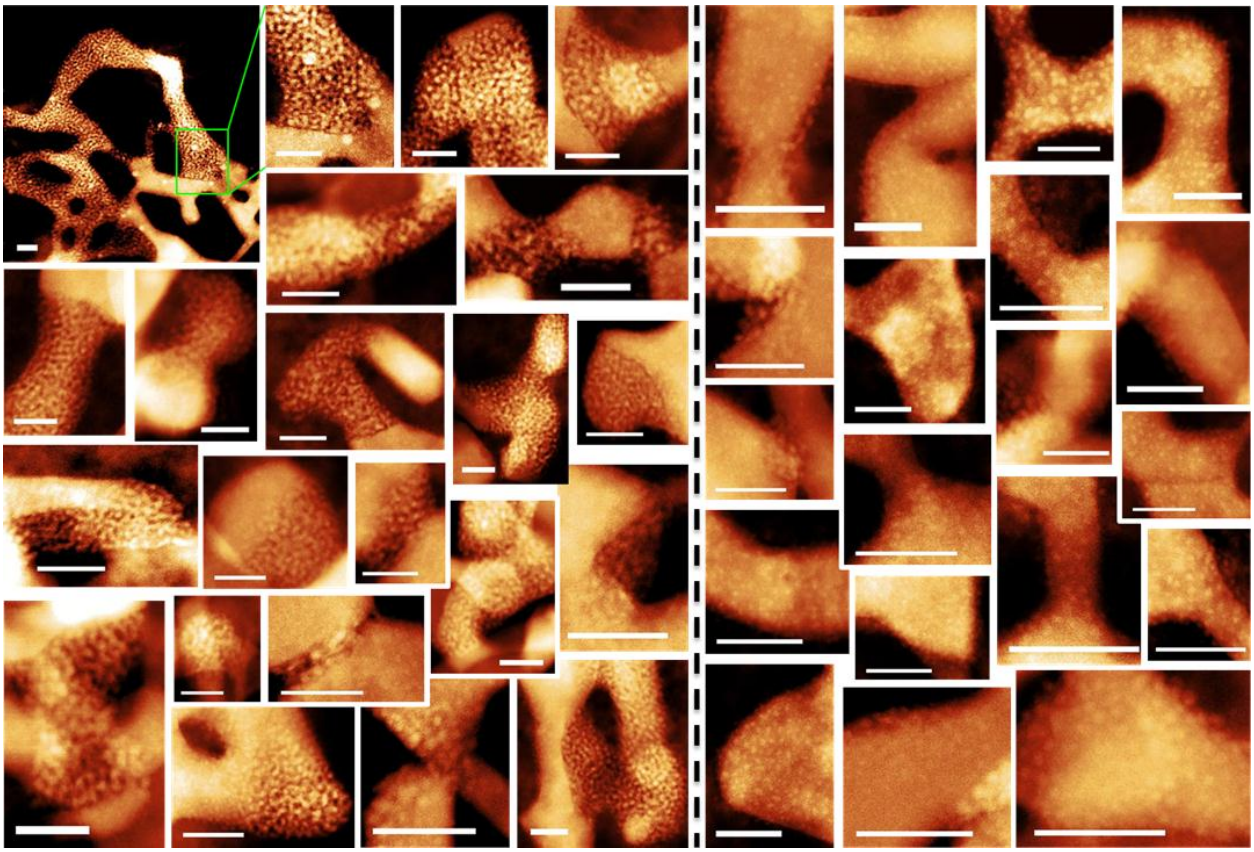

Figure S5. Statistical analysis of reaction modes. STEM images obtained from the 40% discharged sample at 0.1 C-rate showing lithiation *via* Mode B (bulk mode, left of the dashed line, 21 scenarios) or Mode S (shrinking-core mode, right of the dashed line, 19 scenarios). The surface mode probability is thus 47.5% by definition of the surface-reaction events over total events (19/40). Each of the representative images was captured from a large area with the same morphological characteristics, as indicated in the low-magnification image on the top-left. The data acquisition was carried out in a stochastic pattern without any cherry-picking, which ensures the statistical nature of the true reaction modalities. Scale bars, 20 nm.

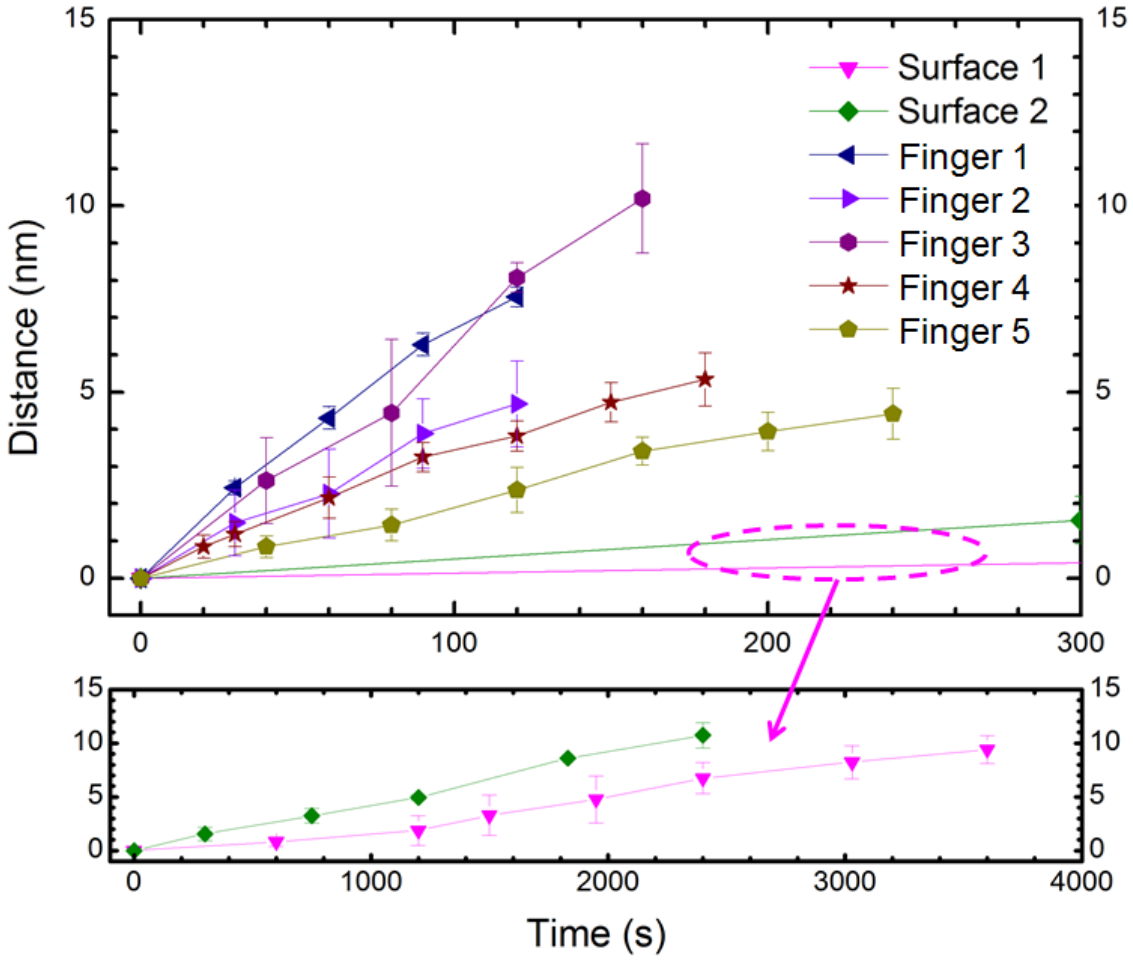

Figure S6. Reaction front propagation in three modes. The curves in the top panel show positions of reaction front as a function of reaction time, which are extracted from multiple *in situ* S/TEM videos. These curves corresponding to different reaction modalities fall into two distinct categories: the fast finger propagations (denoted as finger #1-#5) and extremely slow shrinking-core propagations (denoted as surface #1 and #2) are re-plotted in the left bottom panel, as indicated by the dashed ovals and arrows. By taking the derivatives of these curves, the transient propagation velocities are obtained and plotted in the Figure 2e. The colors and symbols are consistent for corresponding data points in Figure S6 and Figure 2e.

2. Detailed discussion on the DFT calculation and finite element analysis (Figures S7-S9)

2.1 DFT calculation

Lithiation of crystalline NiO is a heterogeneous reaction; local cooperative rearrangement of atoms at the surface of NiO occurs to advance the reaction front. Surfaces of NiO in various crystallographic orientations have drastically different atomic configurations. Such pronounced dissimilarity can readily result in different reaction rates on different orientations. For the heterogeneous reactions involving single crystals, the anisotropy in the rates of reaction is a norm, for instance, drastic anisotropic lithiation has been recently observed in crystalline silicon that lithiation along <110> direction is faster by one order of magnitude than that along other orientations. We first examine the atomic configuration of crystalline NiO to illustrate the origin of the anisotropic reactions along different crystallographic orientations. NiO has a rock-salt structure. Each Ni and O atoms forms a separate face-centered cubic lattice, with the two lattices interpenetrating so as to form a 3D checkerboard structure. Alternately, we may view the structure as a face-centered cubic structure formed by the O frame with octahedral sites occupied by Ni ions. The interstitial tetrahedron sites of the O ions are the energetically favorable positions for Li insertion, with a formation energy of -1.45 eV. Figure 4a depicts the polyhedra of crystalline NiO viewed along the <100>, <110>, and <111> orientations. The atomic structures are tilted slightly to see the three-dimensional out-of-plane features. The gray and red spheres represent Ni and O atoms, respectively. One green Li atom is placed at the tetrahedron site of four O atoms. It is clearly seen that, along both the <110> and <110> orientations, there is an "open channel", that is the lattice space of the FCC structure, for Li transport. In comparison, the <111> direction comprises the most packed orientation in the cubic structure, that the diffusion of Li along such a direction is blocked by its front neighbor. This geometric feature indicates a faster transport rate of Li along the <100> and <110> orientations than that of its unfavorable path along the <111> direction.

For further comparisons, we employed the energetic calculations using the first-principles computational method based on Density Functional Theory (DFT) calculations with Vienna Ab-initio Simulation Package (VASP). We constructed the crystalline NiO models containing 96 atoms with periodic boundary conditions, and along on [100]-[010]-[001] and $[\bar{1}10]-[111]-[11\bar{2}]$ orientations. To model the lithiation along a prescribed orientation, we incrementally inserted Li in the half cell, such that a phase boundary between the lithiated phase and the pristine crystalline NiO was maintained. Li atoms were placed at the energetically favorable positions –at low Li concentrations, the tetrahedron sites of O atoms constituted the intercalation positions for Li insertion. At relatively high Li concentrations, the crystalline structure of the lithiated region is disordered, so we performed Delaunay triangulation to find the largest void size in the lattice to accommodate further insertion of Li. From the energetic perspective, we calculated the formation energies along the <100>, <110>, and <111> directions

at various Li concentrations, to compare the thermodynamic stability of Li insertions along the different crystallographic orientations. We took the energy of crystal NiO (E_{NiO}) and the energy of the Li atom in its bulk form (E_{Li}) as the reference energies, with $E_{nLi\text{-}NiO}$ being the total energy of the system containing n Li atoms in the cell. The formation energy per Li atom E_f(n) was calculated as $E_f(n) = [E_{nLi\text{-}NiO} - E_{NiO} - nE_{Li}]/n$. Figure 4b shows the formation energies for Li insertion along different orientations. It is evident that Li is more favorably inserted along the <100> and <110> orientations than that along the <111> direction. Figure 4b also plots the specific free energy that is defined as the energy per atom in the super cell, which shows the same characteristics that lithiation along the <100> and <110> orientations resulted in more energetically favorable structures. In addition, the volume expansion as a function of the concentration of inserted Li ions was calculated, as shown in Figure S7. After the insertion of two Li ions per NiO unit, the fully lithiated material exhibits a highly disordered structure, and also causes a volumetric strain up to 120%.

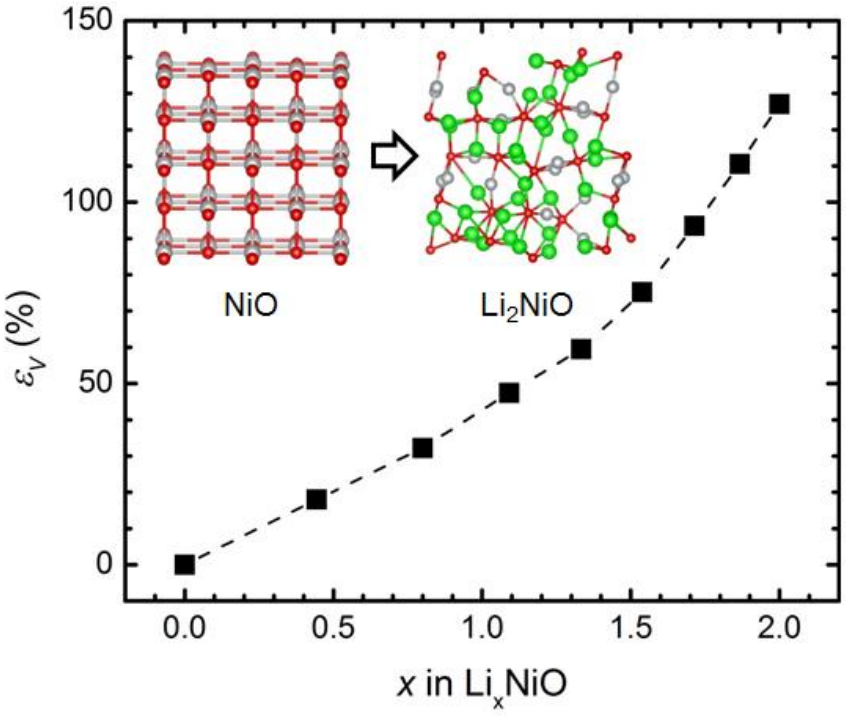

Figure S7. Lithiation-induced volume expansion. The volumetric strain as a function of the concentration of inserted Li ions. The insets show crystal structures changing from well-arranged pristine crystal to the highly disordered lithiated structure. Ni-gray, O-red, Li-green.

2.2 Finite deformation analysis

To accommodate the large expansion (~120%) caused by the conversion reaction of NiO must deform plastically. We propose simplified models with flat or curved reaction interfaces, as illustrated in Figure S8 a and b. When the reaction front is flat, the volumetric change in the lithiated region is accommodated by expansion in the direction normal to the reaction front, while the geometric compatibility in the directions tangential to the phase boundary is maintained. Given the traction-free boundary condition in the direction normal to the reaction front, a material element at the interface is under biaxial compressive stresses. In the course of the phase boundary propagation, freshly lithiated phase is added at the boundary, and previously lithiated material recedes by rigid-body translation, without further deformation. The biaxial stresses in the lithiated NiO remain the compressive yield strength. When the reaction front is curved such as in the Mode S (shrinking-core mode) in Figure 2c, the crystalline core and the lithiated phase form a core-shell structure. Because of the large mismatch strain at the phase boundary, a material element at the reaction front is under compressive stresses. As the reaction front advances, freshly lithiated phase is added at the front, and previously lithiated materials recede. Such a process causes further enlarge of the lithiated shell – however, the further deformation is under three-dimensional constraints. Therefore, a material element at the interface is under triaxial stresses, which distinguishes the stress state in the bulk reaction mode. The triaxiality of the stress field at the reaction front is non-trivial. It is well known that for an elasto-plastic material, the magnitude of the biaxial stresses is upper-limited by the material yield strength, while the value of each stress component in the triaxial stress state can be much larger than the yield strength. Consequently, the triaxial stresses may regulate the lithiation reaction in a more significant manner, as evident in recent noteworthy studies that a sufficiently large pressure at the interface of crystalline silicon could stop the lithiation reaction.

For simplicity, the stress field at the reaction front in the bulk reaction mode may be considered as the equal-biaxial stresses, such that $\sigma_x = \sigma_y = \sigma_y$, where σ_y represents the yield strength of the lithiated phase. We derive the triaxial stress field in the surface reaction mode using the continuum theory of finite deformation. The geometry is represented in Figure S8 c and d. We represent a material element in the reference configuration by its distance *R* from the center. At time *t*, the material element moves to a place at a distance *r* from the center. The function *r(R, t)* specifies the deformation kinematics. Due to the mechanical constraint imposed by the crystalline NiO in the axial direction, the lithiated phase is assumed to deform under the plane-strain conditions. To focus on the main feature, we neglect the elasticity of the lithiated material; we model the lithiated phase as a rigid-plastic material. Consequently, the expansion of lithiated material is entirely due to the lithiation. Consider the shell of the lithiated phase between the radii *A* and *R*. After lithiation, the core radius becomes *a*, and the material element moves to a new position *r*. We assume that lithium is injected slowly and has sufficient time to diffuse

through the lithiated region. The ratio of the volume of the lithiated shell over the volume of pristine phase is represented as β .Thus,

$$R^2 - A^2 + \beta\left(a^2 - A^2\right) = r^2 - a^2. \tag{1}$$

This equation gives the function *r(R, t)* once the kinetics of the reaction front propagation $a(A)$ is given. Let's take $f(A) = (1+\beta)\left(a^2 - A^2\right)$ Therefore $f(A)$ fully specifies the kinematics of the lithiated shell,

$$r = \sqrt{R^2 + f(A)}. \tag{2}$$

The stretches can be calculated as

$$\lambda_r = \frac{\partial r}{\partial R} = \frac{R}{r}, \quad \lambda_\theta = \frac{r}{R}, \quad \lambda_z = 1. \tag{3}$$

By neglecting the elastic deformation of the lithiated phase, the total expansion is only accommodated by the plastic deformation when the reaction front advances. We calculate the strain components from the stretches,

$$\varepsilon_r^p = \varepsilon_r = \log\lambda_r, \quad \varepsilon_\theta^p = \varepsilon_\theta = \log\lambda_\theta, \quad \varepsilon_z^p = \varepsilon_z = \log\lambda_z. \tag{4}$$

To calculate the stress field, one has to consider the incremental plastic deformation with respect to time. Given Eq. (3) and (4), we obtain that

$$\delta\varepsilon_r^p = -\frac{1}{2r^2}\delta f,\ \delta\varepsilon_\theta^p = \frac{1}{2r^2}\delta f,\ \delta\varepsilon_z^p = 0. \tag{5}$$

The equivalent plastic strain increment is

$$\delta\varepsilon_{eq}^p = \sqrt{\frac{2}{3}\delta\varepsilon_{ij}^p\delta\varepsilon_{ij}^p} = \frac{2}{\sqrt{3}r^2}\delta f. \tag{6}$$

We adopt the flow rule

$$s_{ij} = \frac{2}{3}\frac{\sigma_Y}{\delta\varepsilon_{eq}^p}\delta\varepsilon_{ij}^p. \tag{7}$$

where s_{ij} is the deviatoric stress, defined as $s_{ij} = \sigma_{ij} - \frac{1}{3}\sigma_{ii}$. Therefore,

$$s_r = -\frac{\sqrt{3}}{3}\sigma_Y, s_\theta = \frac{\sqrt{3}}{3}\sigma_Y, s_z = 0. \tag{8}$$

and

$$\sigma_r - \sigma_\theta = s_r - s_\theta = -\frac{2\sqrt{3}}{3}\sigma_Y. \tag{9}$$

Consider the force balance of a material element in lithiated NiO

$$\frac{\partial\sigma_r}{\partial r} + \frac{\sigma_r - \sigma_\theta}{r} = 0. \tag{10}$$

the radial stress can be obtained by integrating Eq. (10), it gives,

$$\sigma_r = -\frac{2\sqrt{3}}{3}\sigma_Y \log r + D. \tag{11}$$

The integration constant D is determined by the traction-free boundary condition, $\sigma_r(b, t) = 0$, such that

$$\sigma_r = -\frac{2\sqrt{3}}{3}\sigma_Y \log\frac{r}{b}$$
$$\sigma_\theta = -\frac{2\sqrt{3}}{3}\sigma_Y\left(\log\frac{r}{b}+1\right) \tag{12}$$
$$\sigma_z = -\frac{2\sqrt{3}}{3}\sigma_Y\left(\log\frac{r}{b}+\frac{1}{2}\right).$$

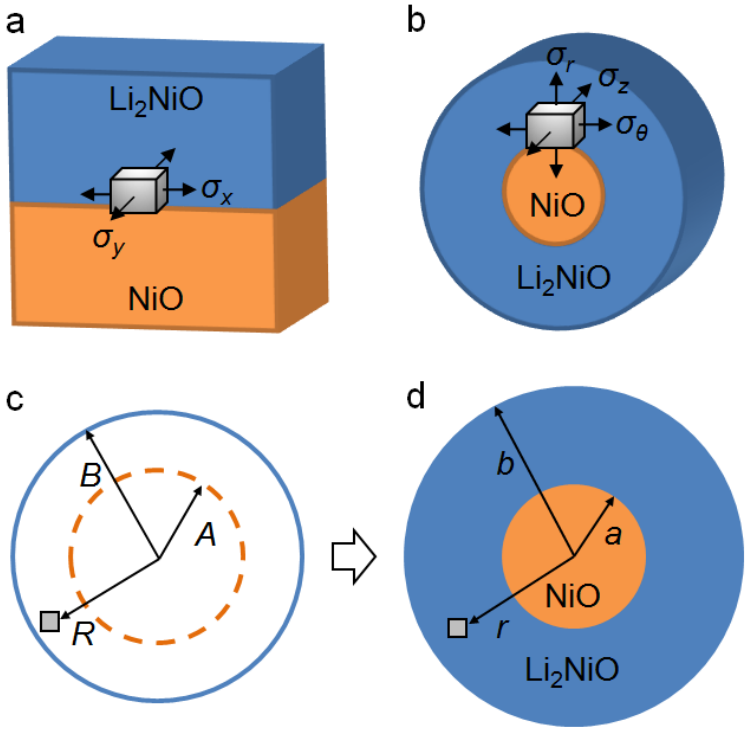

Figure S8. Analytical model for finite deformation. The stress states at the (a) flat or (b) curved reaction interface. A material element at the phase boundary is represented by the gray cube. For lateral propagation of the reaction front without curvature, the material element is under a biaxial stress field. For the circular propagation of the reaction front, as the reaction advances, deformation of the material element is under three-dimensional constraints, which induces a triaxial stress field. (c) In the reference state, an element of lithiated NiO is represented by its distance from the center R. The radius of the unlithiated NiO (core) is A, and the radius of the lithiated phase (shell) B. (d) At time t, NiO in the shell between the radii A and a is lithiated, and the element R moves to a new position of radius r.

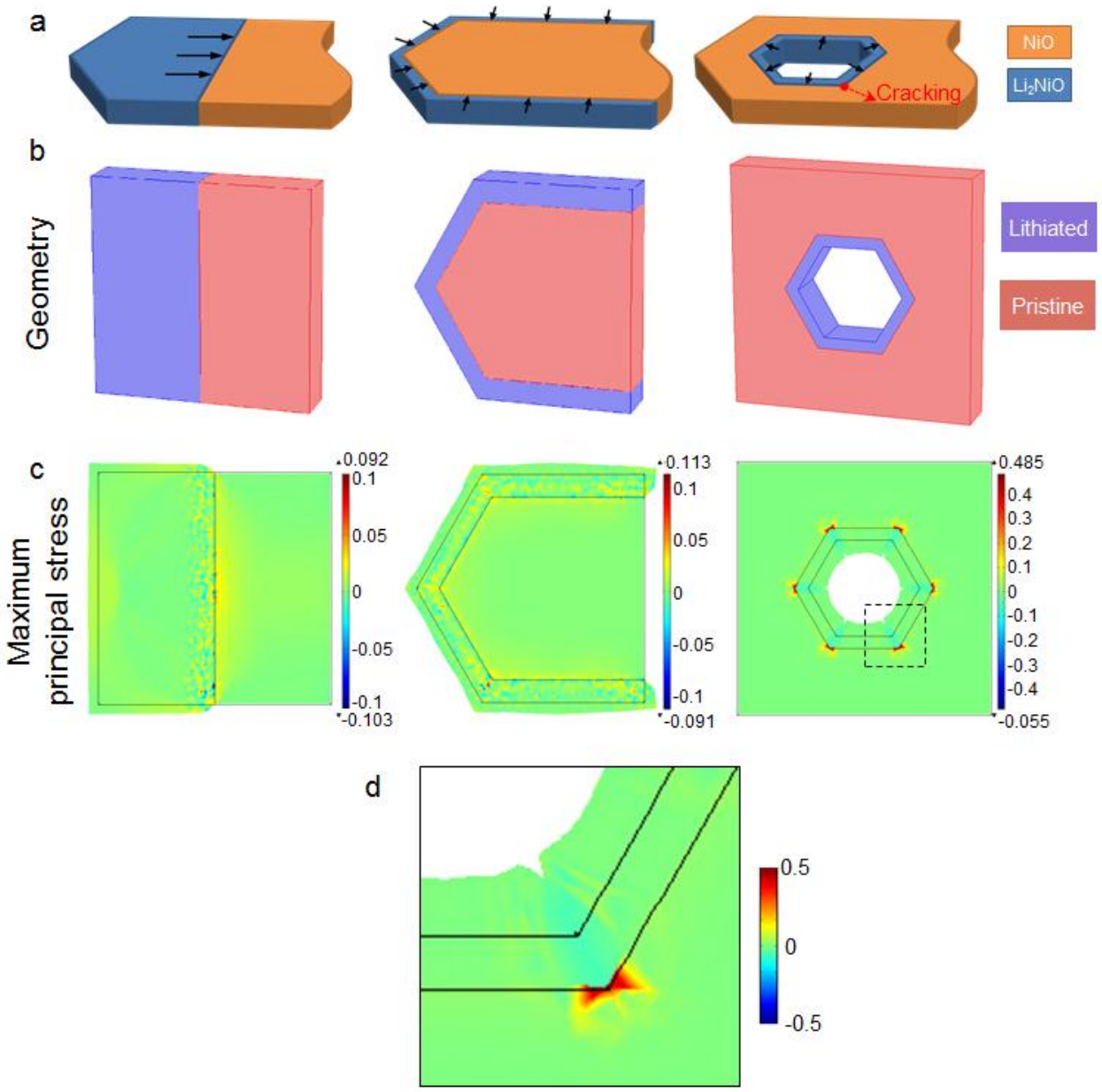

Figure S9. Finite element simulation of stress distribution after lithiation. (a) Schematic models showing lithiation propagation fronts through bulk and surfaces of a NiO nanosheet. (b) Geometries of three representative reaction scenarios: bulk reaction at a flat interface, surface reaction at the outer edges of a sample slab, and surface reaction at the inner edges of a hexagonal hole, respectively. Pristine region in salmon, lithiated region in purple. (c) The maximum principal stress of the complete lithiation state induced by 120% volumetric strain. The stresses are present in unit of the Young's modulus of NiO ($E_{NiO} = 1$). (d) An enlarged view of the dashed box in (c) shows a large tensile stress concentrated at the upfront corner of the unreacted region.

For better evaluating the effect of stress on the reaction modalities and kinetics, we carried out the finite element simulation using COMSOL Multiphysics software suite for the representative scenarios proposed in Figure S9a. We retain the structural characteristics of these situations, namely bulk reaction at a flat interface, surface reaction at the outer edges of a sample slab, and surface reaction at the inner edges of a hexagonal hole, respectively, and use the simplified geometries, as illustrated in Figure S9b. The dimensions for each model are $100\times100\times20$ nm^3. The 120% volumetric strain was applied to the lithiated regions, and the whole material was allowed to take plastic deformation to accommodate the strain. Figure S9c shows the final geometries with plastic deformation and the maximum principal stresses of the three cases. The calculated stresses are measured in unit of the Young's modulus of NiO ($E_{NiO} = 1$). For the first two situations, the lithiated regions are able to expand to free spaces and the unreacted regions are under relatively small tensile stresses. But in the third case, it is found that the much larger tensile stresses are concentrated at the corners, where cracks may likely to be generated and then propagate to the unlithiated regions.

3. Description of Supporting Movies 1–5

3.1 Movie captions

Supporting Movie 1. *In situ* TEM imaging to show a slow circumferential percolation *via* the shrinking-core mode (near surface reaction then further thickening, the same area as in Figure 2c). The original live video was recorded in the TEM mode with exposure time of 0.1s (refreshing rate of 10 frames per second). The movie clip is accelerated by 150 times.

Supporting Movie 2. *In situ* HAADF-STEM imaging to show a transformation from a Mode S (shrinking-core reaction) to Mode B (bulk propagation) *via* finger mode, the same area as in Figure 2d. The original live video was recorded in the STEM mode at the scanning rate of 1 frame per second. The movie clip is accelerated by 30 times.

Supporting Movie 3. *In situ* TEM imaging to show lithiation *via* Mode B (bulk mode). The original live video was recorded in the TEM mode with exposure time of 0.1s (refreshing rate of 10 frames per second). The movie clip is accelerated by 5 times.

Supporting Movie 4. *In situ* electron diffraction of a large scale of NiO nanosheet during a complete lithiation cycle. The original live video was recorded in TEM-Diffraction mode with exposure time of 0.1s (refreshing rate of 10 frames per second). The movie clip is accelerated by 20 times.

Supporting Movie 5. Three-dimensional STEM reconstructed tomography of a NiO nanosheet after an *in situ* lithiation process with formation of fingers.

3.2 Detailed description

Movie 1 displays a lithiation process *via* the shrinking-core mode. The region of interest focuses on the edge of a NiO nanosheet with a small piece attached. The lithium ions and electrons are supplied from the bottom-right direction. Here, the lithiation proceeds through an extremely slow course, during which the reaction fronts moves circumferentially from the surface of the materials towards the center. Therefore, we define this type of lithiation process as the shrinking-core mode, which does not include any side electrochemical reactions on the surface of the electrode material. After 3600s, the lithiation has not been finished, as there is still crystalline NiO remaining inside the reacted regions.

Movie 2 displays a scenario where finger mode dominates the lithiation process. The region of interest focuses on an inner area of a NiO nanosheet, which includes a few hexagonal holes. The

lithium ions and electrons are supplied from the bottom-right side of the field of view. The lithiation through the finger mode is much faster than that *via* shrinking-core mode. At the early stage of the lithiation, near-surface reactions occur at the inner edges of some hexagonal holes. Then, a few “finger”-like features appear within the NiO nanosheet and quickly propagate through the slab to generate penetration channels that promote further rapid lithiation. Penetration fingers typically form at one corner of a hexagonal hole, then propagates through a random route, and finally ends up at another corner of a hexagonal hole or merges with other wedges. After 440s, the reaction is approached the end, as the lithiated area covers the most of the electrode regions. It is worth to note that one could observe the shrinking-core mode in some areas of this video.

Movie 3 displays a lithiation process *via* the I→I transition (or bulk mode). In the field of view, a piece of NiO nanosheet slab suspends on the lacy carbon film, through which lithium ions and electrons are continuously supplied and efficiently transported to the interior region of NiO after penetration channels have been established (not shown in this field of view). As the lithiation progresses, the reaction front traverses across the interior bulk region, along with the volume expansion and the consequently caused warp and distortion to accommodate the local stresses, which are indicated as the bending contours at the reaction boundaries. After 68s, the entire NiO nanosheet is completely lithiated.